

Scattering Shadows

Thomas Curtright[§] and Gaurav Verma^b

Department of Physics, University of Miami, Coral Gables, FL 33124

Abstract

We discuss the regions forbidden to classical scattering trajectories by repulsive potentials. We give explicit results for the asymptotic form of these regions, far from the scattering center, in terms of the scattering angle function.

Introduction

Consider particles of energy $E > 0$ incident on a repulsive potential V with $E < V_{\max}$. The resulting classical scattering trajectories due to smoothly varying, continuous potentials may exhibit “shadows” (classically forbidden regions) [1]. The structure of these shadows is discussed here, in a non-relativistic context for various isotropic potentials, with particular attention to their asymptotic form.

If $V(r)$ is falling monotonically but is non-vanishing for *all* distances from the fixed scattering center, the transverse size of the scattering shadow may grow without bound as the downstream distance increases in the forward direction, even if the potential becomes arbitrarily weak at large distances. This is demonstrated here for various potentials. In our opinion, this accounts for divergent total cross-sections in terms of physical effects more easily visualized and more intuitively understood than, say, angular integrations of differential cross-sections with singular small angle behavior, or integrations over unbounded impact parameters.

Classical Analysis

All scattered particle trajectories are determined by the usual methods of energy and angular momentum conservation, as exhibited here:

$$E = \frac{m}{2} \left(\frac{dr}{dt} \right)^2 + \frac{L^2}{2mr^2} + V(r) , \quad L^2 = m^2 r^2 \left(\frac{d\vartheta}{dt} \right)^2 \quad (1)$$

where r is the distance of the particle from the fixed scattering center, and the angle ϑ is measured from the incoming direction of the particle. (Please see the scattering diagram in Appendix A.) If the particle’s asymptotic speed is v and its impact parameter is s , then

$$E = mv^2/2 , \quad L^2 = m^2 v^2 s^2 \quad (2)$$

If a is the closest approach distance to the scattering center (i.e. r at periapsis) and $h = a|_{s=0}$ is the closest approach distance for a head-on collision, with $h > 0$ for $E < V_{\max}$, then

$$E = V(h) = \frac{L^2}{2ma^2} + V(a) , \quad L^2 = 2ms^2V(h) , \quad 1 = \frac{s^2}{a^2} + \frac{V(a)}{V(h)} \quad (3)$$

$$\frac{m}{2} \left(\frac{dr}{dt} \right)^2 = V(h) \left(1 - \frac{s^2}{r^2} \right) - V(r) , \quad \frac{d\vartheta}{dr} = \frac{d\vartheta/dt}{dr/dt} = \frac{s}{r^2} \frac{(\mp 1)}{\sqrt{1 - \frac{s^2}{r^2} - \frac{V(r)}{V(h)}}} \quad (4)$$

with \mp before/after periapsis and where ϑ is again measured from the incident direction (say, the $-z$ axis).

[§]curtright@miami.edu

^bgxv211@miami.edu

The scattering trajectories, as determined by $\vartheta(r)$, therefore reduce to quadratures. Explicitly, upon changing variables to $\sin \phi \equiv a/r$,

$$\vartheta(r) = \sqrt{1 - \frac{V(a)}{V(h)}} \int_0^{\arcsin(a/r)} \frac{1}{f(h, a, \phi)} d\phi \quad \text{for incoming } r \geq a \quad (5)$$

$$\vartheta(r) = \sqrt{1 - \frac{V(a)}{V(h)}} \int_{\arcsin(a/r)}^{\pi} \frac{1}{f(h, a, \phi)} d\phi \quad \text{for outgoing } r \geq a \quad (6)$$

where the denominator of the integrand is

$$f(h, a, \phi) = \sqrt{1 + \frac{V(a) \sin^2 \phi - V(a/\sin \phi)}{V(h) \cos^2 \phi}} \quad (7)$$

For repulsive potentials that fall monotonically to zero, f is always real and positive for all $\phi \in [0, \pi]$. The scattering angle Θ as measured from the forward direction is given by $\Theta = \pi - 2\vartheta(a)$, hence

$$\Theta = \pi - \sqrt{1 - \frac{V(a)}{V(h)}} \int_0^{\pi} \frac{1}{f(h, a, \phi)} d\phi \quad (8)$$

Interesting examples are provided by inverse-power potentials, namely,

$$V_n(r) = \frac{\kappa}{r^n} \quad (9)$$

with $\kappa > 0$ and $n > 0$, for which the post-periapsis angle is

$$\vartheta_n(r) = \sqrt{1 - \frac{h^n}{a^n}} \int_{\arcsin(a/r)}^{\pi} \frac{d\phi}{\sqrt{1 + \frac{h^n \sin^2 \phi - \sin^n \phi}{a^n \cos^2 \phi}}} \quad \text{for outgoing } r \geq a \quad (10)$$

In particular, for outgoing $r \geq a$, Coulomb potential results are

$$\vartheta_1(r) = 2 \arctan\left(\sqrt{1 - h/a}\right) + 2 \arctan\left(\frac{\sqrt{1 - h/a} \sqrt{1 - a/r}}{\sqrt{1 + (a - h)/r}}\right) \quad (11)$$

$$\Theta_1 = \pi - 2\vartheta_1(a) = \pi - 4 \arctan\left(\sqrt{1 - h/a}\right) \quad (12)$$

and inverse-square potential results are

$$\vartheta_2(r) = \sqrt{1 - h^2/a^2} (\pi - \arcsin(a/r)) \quad (13)$$

$$\Theta_2 = \pi - 2\vartheta_2(a) = \pi \left(1 - \sqrt{1 - h^2/a^2}\right) \quad (14)$$

Some representative trajectories for these two particular cases are given in the Figures of the following Section. Depending on the value of the impact parameter, at specific points each trajectory is locally tangent to an envelope curve, as is evident in the Figures.

By definition, for these examples or for any other repulsive potentials, at a fixed energy $E < V_{\max}$ the *scattering shadow* is the region containing the scattering center and bounded by the trajectory envelope. This is a region into which a *classical* particle with energy E is forbidden to travel for *all* impact parameters s and corresponding angular momenta L . Note that the length scales for this region are energy dependent, as set by the value of h for the potential in question. The envelope can be obtained by a minimization procedure, in various ways, as described in Appendix B.

Exemplary Trajectories

First, consider $V_1 = \kappa/r$. For this repulsive Coulomb scattering example, the envelope of the trajectories is given exactly by [2, 3]

$$\frac{z}{h} = -1 + \frac{1}{4} \left(\frac{y}{h} \right)^2 \quad \text{where} \quad E = \frac{\kappa}{h} \quad (15)$$

The envelope is plotted along with representative trajectories in Figure 1.

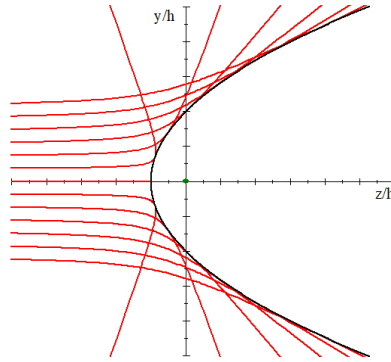


Fig.1: Coulomb scattering trajectories shown in red for fixed E and various L . In this case, the (black) trajectory envelope is just a parabola.

Next, consider $V_2 = \kappa/r^2$. For this inverse-square potential, in Figure 2 the trajectories are only shown *after* periapsis, and the envelope curve is *not* plotted. The envelope is not a parabola in this case.

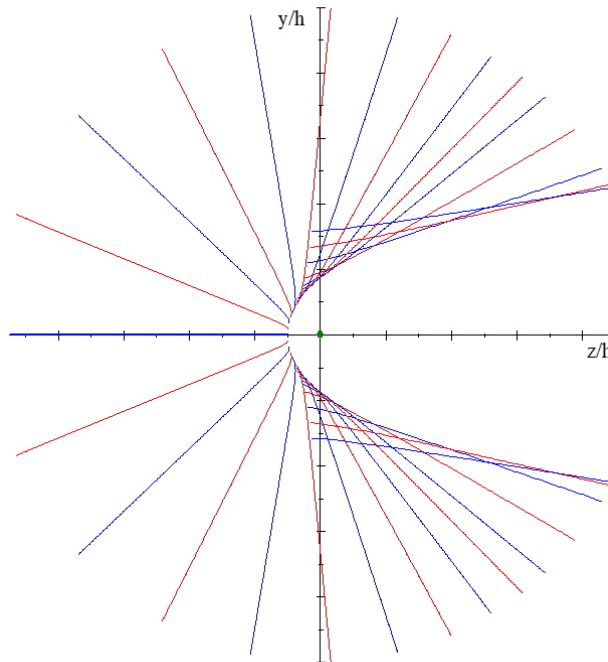


Fig. 2: Outgoing inverse-square potential scattering trajectories for fixed E and various L , plotted in alternating red and blue colors. Although it is not plotted, a trajectory envelope is clearly discernible.

Analytic Shadow Procedures

In principle, the shadow can be obtained analytically by the minimization procedures described graphically in Appendix B. The third procedure described therein is readily adapted to the Coulomb and inverse-square potentials, given the explicit results for $\vartheta_1(r)$ and $\vartheta_2(r)$ as exhibited above. For a given energy, hence a given h , and for a fixed r , the procedure is to minimize ϑ by varying s , hence by varying a .

For the Coulomb potential an elementary expression is obtained for the critical a .

$$\frac{\partial}{\partial a}\vartheta_1(r) = 0 \implies a = \frac{1}{2}h + \frac{1}{2}\sqrt{h(4r - 3h)} \quad (16)$$

Evaluating $\vartheta_1(r)$ at this critical a then gives the enveloping curve solely as a function of r , for the chosen h . The result is most easily expressed as $z = -r \cos \vartheta_1(r)$ written as a function of $y = r \sin \vartheta_1(r)$, as given in (15) and shown as the parabola in the accompanying Figure 1.

For other inverse-power potentials the procedure is the same, but the final result is not so simple. This is due to lack of a closed form expression for the critical a as a function of r , in contrast to the result in (16). The inverse-square potential illustrates this difficulty. The condition to determine the envelope curve is

$$\frac{\partial}{\partial a}\vartheta_2(r) = 0 \implies a(a^2 - h^2) = h^2\sqrt{r^2 - a^2} \left(\pi - \arcsin \frac{a}{r} \right) \quad (17)$$

While the last equation is a fairly simple, closed-form, analytic result, the solution for a is not. Series solutions for $a(r)$ can be obtained, say, by expanding about the $a = h$ head-on collision.¹ But in general, for $a = O(h)$ numerical results are more useful. For example, with dimensionless variables $\rho = r/h$ and $\alpha = a/h$, the envelope condition for $\rho = 2$ is $\sqrt{\rho^2 - \alpha^2} \left(\pi - \arcsin \frac{\alpha}{\rho} \right) = (\alpha^2 - 1) \alpha \Big|_{\rho=2}$. The numerical solution is $\alpha = 1.6150$, and therefore $(z/h, y/h) = (-\rho \cos \vartheta_2(r), \rho \sin \vartheta_2(\rho)) \Big|_{\rho=2, \alpha=1.615} = (0.31479, 1.9751)$.

Figure 3 plots several numerical points (circled in red) for the upper branch of the shadow boundary surrounding the fixed scattering center located at the origin (green).

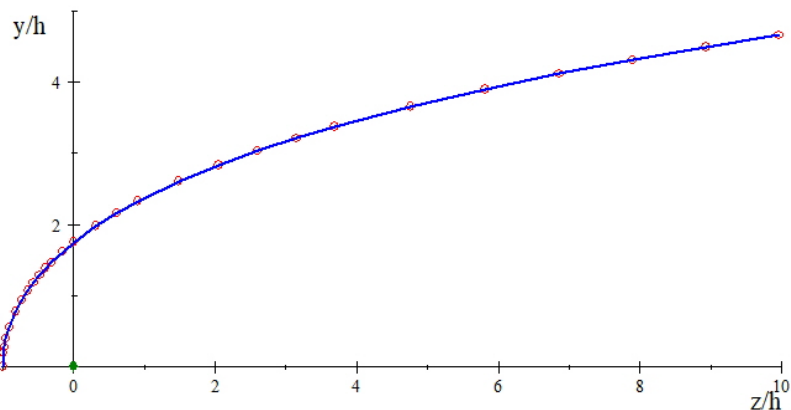


Fig. 3: Numerically computed points on the trajectory envelope for the inverse-square potential, with an interpolating (blue) curve.

However, in lieu of numerical analysis, far from the scattering center in the downstream direction ($+z$ in the Figure) the asymptotic form of the envelope can often be obtained as a simple closed-form expression.

¹For all repulsive potentials considered in this paper, near to $z = -h$ the envelope is approximated by a parabolic function of y , similar to (15).

Exemplary Asymptotic Behavior

The asymptotic form of the envelope, for $z \gg h$, follows from the behavior of trajectories for small scattering angles, which are in turn the result of large impact parameters. For $V_n(r) = \kappa/r^n$, with $\kappa > 0$ and $n > 0$, the small scattering angle behavior is

$$\Theta(s) \underset{s \gg h}{\sim} \frac{h^n}{s^n} b_n \ll 1, \quad b_n = \sqrt{\pi} \Gamma\left(\frac{n+1}{2}\right) / \Gamma\left(\frac{n}{2}\right) \quad (18)$$

as shown in Appendix C. For incident particles with *any* impact parameters striking such continuous repulsive potentials that fall off smoothly with distance, after passing the point of periapsis the trajectories eventually approach straight lines. Moreover, for *large* impact parameters these eventual straight lines are given simply by

$$y \underset{z \gg s \gg h}{\sim} s + z \tan \Theta(s) \sim s + z \Theta(s) \quad (19)$$

where z is the downstream coordinate along the incident beam axis, y is the coordinate transverse to that axis, and Θ is the scattering angle. In the first step exhibiting the asymptotic behavior the intercept of the trajectory has been approximated by just s , while in the second step the smallness of the scattering angle has also been used, both steps being good approximations for large impact parameters.

One way to obtain the envelope for the trajectories is to minimize y^2 at a fixed z by varying s . The asymptotic behavior of the envelope then follows from the condition $0 = \partial y / \partial s \sim 1 + z \Theta'(s)$. Thus, for the V_n potential,

$$z \sim -\frac{1}{\Theta'} = \frac{s}{n\Theta} = \frac{s^{n+1}}{nh^n b_n}, \quad s \sim (nh^n b_n z)^{1/(n+1)} \quad (20)$$

The asymptotic form of the envelope is then obtained by evaluating y subject to this last relation between s and z . The result is

$$\frac{y_{\text{env}}}{h} \underset{z \gg s \gg h}{\sim} \frac{(n+1)s}{nh} \sim c_n \left(\frac{z}{h}\right)^{1/(n+1)} \quad (21)$$

for the V_n potential, where²

$$c_n = \frac{n+1}{n} (nb_n)^{1/(n+1)} = \frac{n+1}{n} \left(\frac{n\sqrt{\pi} \Gamma\left(\frac{n+1}{2}\right)}{\Gamma\left(\frac{n}{2}\right)} \right)^{1/(n+1)} \quad (22)$$

For example: $c_1 = 2$, $c_2 = \frac{3}{2}\pi^{1/3} = 2.19689$, $c_3 = \frac{4}{3}6^{1/4} = 2.08678$, $c_4 = \frac{5}{4}(3\pi)^{1/5} = 1.95778$, and $c_\infty = 1$. The maximum c_n occurs at $n = 1.797296395$, for which $c_n|_{n=1.797296395} = 2.202842270$. Therefore, for any finite $n > 0$ the transverse size of the shadow grows without bound as z increases.

In particular, for the inverse-square potential,

$$y_{\text{env}}/h \underset{z \gg h}{\sim} \frac{3}{2} (\pi z/h)^{1/3} \quad (23)$$

This approximation to the envelope curve is significantly below the actual envelope for $z = O(h)$, as should be expected since it vanishes at $z = 0$. But beyond that, this leading asymptotic term is also too high by a small amount for large z/h , as is evident in Figure 4. Nevertheless, the difference gives a relative error that is negligible for very large z/h , and that goes to zero as $z/h \rightarrow \infty$. In fact, the first correction to the leading asymptotic behavior of the envelope for inverse-square scattering³ is given by $-\frac{3}{8} \frac{1}{(\pi z/h)^{1/3}}$. Or, upon incorporating this into a simple Padé approximant, an improved asymptotic approximation is

$$y_{\text{env}}/h \underset{z \gg h}{\sim} \frac{\frac{3}{2} (\pi z/h)^{1/3}}{1 + \frac{1}{4} (h/\pi z)^{2/3}} \quad (24)$$

Again as is evident in Figure 4, for $z/h > 10$ or so, this gives a better fit to the numerically exact curve.

²Compare this result to the area of a unit sphere in N spatial dimensions: $\Omega_N = \frac{2\pi^{N/2}}{\Gamma(N/2)}$ so $c_n = \frac{n+1}{n} \left(n\pi \frac{\Omega_n}{\Omega_{n+1}} \right)^{1/(n+1)}$.

³Derivation of this correction is left as an exercise for the interested reader.

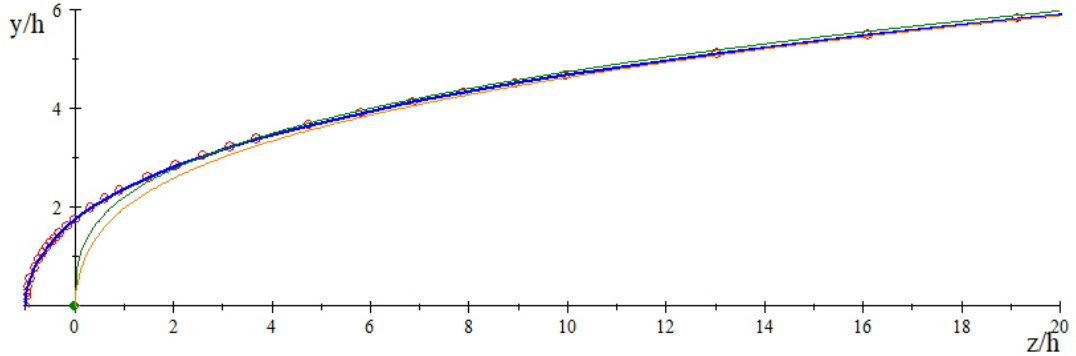


Fig. 4: Numerically computed points (encircled in red) on the trajectory envelope for the inverse-square potential, with an interpolating (blue) curve. The green curve is the leading asymptotic behavior, (23), while the orange curve is a correction to this using a Padé approximant, (24).

As another example, consider a Yukawa potential.

$$V(r) = \frac{\kappa}{r} \exp(-r/\lambda) \quad (25)$$

In this case the relevant asymptotic behavior is given by the following, again as taken from Appendix C.

$$\Theta \underset{a \approx s \gg h, \lambda}{\sim} \sqrt{\frac{8\pi}{s\lambda}} h \exp\left(-\frac{s}{\lambda}\right), \quad \frac{d}{ds} \Theta \underset{a \approx s \gg h, \lambda}{\sim} -\frac{1}{\lambda} \Theta \quad (26)$$

$$z \sim -\frac{1}{\Theta'} \sim \frac{\lambda}{\Theta} \sim \frac{\lambda}{h} \sqrt{\frac{s\lambda}{8\pi}} \exp\left(\frac{s}{\lambda}\right), \quad s \sim \lambda \ln(z/\lambda) \quad (27)$$

The large z form of the scattering envelope follows by the same methods as used for the inverse-power potentials.

$$y_{\text{env}} \underset{z \gg a \approx s \gg h, \lambda}{\sim} s + z \Theta(s) \sim \lambda \ln(z/\lambda) + h \sqrt{\frac{8\pi}{\ln(z/\lambda)}} \sim \lambda \ln(z/\lambda) + O\left(\frac{1}{\sqrt{\ln(z/\lambda)}}\right) \quad (28)$$

For fixed $\lambda > 0$ the transverse size of the shadow still grows without bound as z increases, but only as $\ln z$, hence more slowly than for any inverse-power potential V_n with $n > 0$.

Total Cross-sections

It is well-known that the “total” cross-section $\sigma = \int \left(\frac{d\sigma}{d\Omega}\right) d\Omega$ is *infinite* for the Coulomb potential when computed classically. It is perhaps less well-known that this is true for *all* inverse-power potentials V_n with $n > 0$. Moreover, it is perhaps even less well-known that σ is also infinite for the Yukawa potential when computed *classically*. There are at least three ways to obtain these divergent total cross-sections. These involve: Impact parameter integrals; Integrations over singular small angle behavior; Scattering shadows. The amount of insight and intuition provided by these three approaches differs significantly, increasing with the listed ordering, in our opinion.

The first way to understand infinite σ is to compute the total cross-section in terms of the impact parameter, e.g. $\sigma = 2\pi \int s ds$ in three spatial dimensions, and to use the fact that the upper limit of the integral is ∞ if the potential is non-zero, albeit arbitrarily small, for all finite distances no matter how far from the fixed scattering center. However, this computation reveals next to nothing about the detailed structure of the potential.⁴

⁴For anyone seeking to find an elementary physics example that uses category theory ... well ... this is an “abstract nonsense” proof if we ever saw one.

A more informative way to understand infinite σ is to consider the small angle behavior of $d\sigma/d\Omega$. If this differential cross-section is sufficiently singular as $\Theta \rightarrow 0$ then again σ is infinite due to the divergence of the integral $\int_0^\pi (d\sigma/d\Theta) d\Theta$. This is the case for all the aforementioned repulsive inverse-power potentials and also for the Yukawa potential, when computed classically, as can be seen using the small angle scattering results in Appendix C. This method encodes more information about the potential than the impact parameter calculation, since it requires precise knowledge about scattering behavior at small angles. But, in our opinion, this computation is not easily visualized and does not impart much physical intuition. Moreover, this approach relies on an infinite limit, namely, it is necessary that the impact parameter $s \rightarrow \infty$ to produce $\Theta \rightarrow 0$ for the repulsive potentials under consideration.

On the other hand, the scattering shadow is a very intuitive way to understand the physics that underlies σ . Again in our opinion, this approach accounts for divergent total cross-sections in terms of effects very easily visualized, namely, the unbounded growth of the shadow’s transverse area as the downstream distance from the scattering center increases. In addition, this third way of thinking provides a clear picture of classical physics effects even when observations are made at *finite* downstream distances since the shadow region is well-defined for all $z > -h$. Thus, once in hand, the scattering shadow admits greater physical transparency, visualization, and intuition than provided by either the impact parameter or scattering angle considerations alone.

Summary

The structure of scattering shadows (classically forbidden regions) was discussed here, in a non-relativistic context for various isotropic potentials, with particular attention to their asymptotic form. For the monotonically falling, repulsive potentials considered, the transverse size of the scattering shadow was shown to grow without bound as the downstream distance increased in the forward direction, even though the potentials became arbitrarily weak at large distances. This shadow growth accounted for divergent total cross-sections in terms of physical effects more easily visualized and more intuitively understood than either angular or impact parameter integrations.

That said, as anyone familiar with light waves or quantum mechanics already knows, these shadows do *not* persist when point-particle classical mechanics is set aside for more accurate descriptions of scattering processes. Indeed, penetration of the classical shadow by diffracted light to form Poisson’s spot in the forward direction was the experimentum crucis that distinguished electromagnetic waves from Newton’s particle theory of light [8]. Similar phenomena have been observed for molecular beams [9], thereby providing further evidence in favor of quantum mechanics.

Perhaps the situation was best described in another context:

“But in the end it’s only a passing thing, this shadow ...” — Sam, in *The Lord of the Rings*.

Nevertheless, to make a clear distinction between such alternative scattering theories, a full appreciation of classical mechanics is required. Hopefully the discussion given here has increased that appreciation.

Acknowledgements

Discussions with Tom Kephart were greatly appreciated. This work was supported in part by the United States Social Security Administration.

Appendix A: Scattering Diagram

Variables used to describe the classical scattering process are illustrated in Figure 5 for a particular trajectory, as shown in blue.

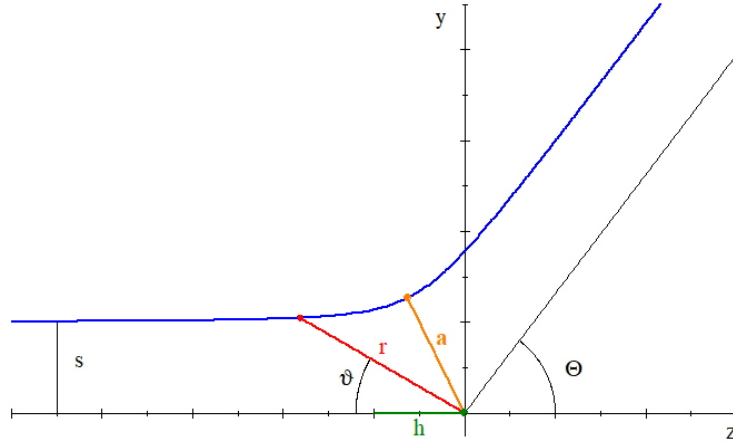


Fig. 5: The classical scattering diagram.

The coordinate frame has been chosen so that the trajectory lies in the yz -plane, and the particle with energy E is incident from infinity with initial asymptotic velocity $\vec{v} = \sqrt{2mE} \hat{z}$. For the trajectory shown, the impact parameter is s , the periapsis is a , and the scattering angle is Θ . The closest approach distance for a head-on collision with the same energy E is shown in the diagram as h .

Appendix B: Minimization Procedures

For a given energy, the envelope can be obtained by varying the impact parameter s (hence varying $L = \sqrt{2mE}s$) to find the minimum transverse distance y at a fixed value of z , as shown graphically by trajectories intersecting the vertical green lines in Figure 6.

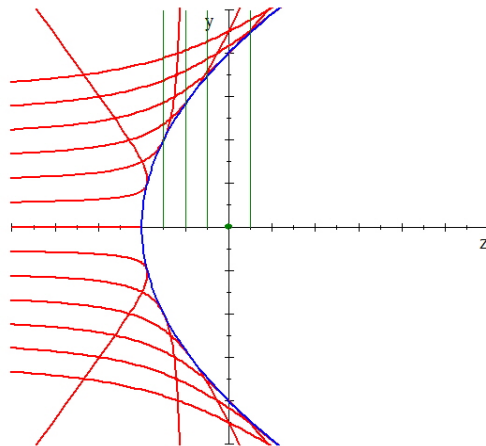


Fig. 6: Scattering trajectory envelope for fixed E , viewed as minimum y for fixed z .

Another, equivalent procedure to find the envelope is by varying the impact parameter s to find the minimum radial distance r at a fixed value of the polar angle θ , as shown graphically by trajectories intersecting the green rays in Figure 7.

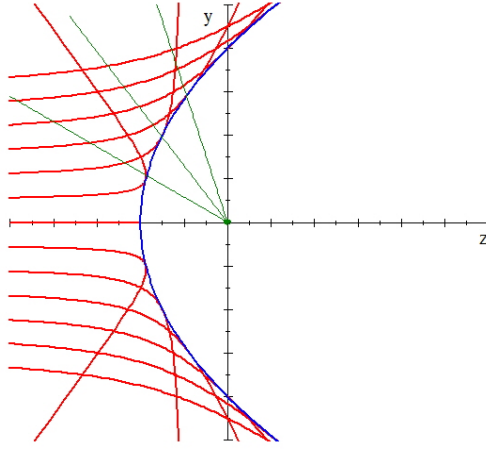


Fig. 7: Scattering trajectory envelope for fixed E , viewed as minimum r for fixed θ .

Yet another procedure to find the envelope is by varying the impact parameter s to find the minimum polar angle θ at a fixed value of r , as shown graphically by trajectories intersecting the green circles in the following Figure 8.

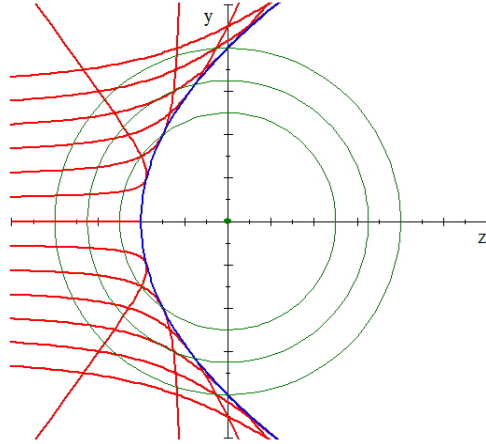


Fig. 8: Scattering trajectory envelope for fixed E , viewed as minimum θ for fixed r .

Appendix C: Small Angle Scattering

For large impact parameters $s \gg h$, hence periapsis distances $a \gg h$ and therefore small Θ , the scattering angle integral (8) may be approximated by expanding the integrand to first nontrivial order in $V(a)/V(h)$. Thus

$$\Theta \underset{a \gg h}{=} \pi - \sqrt{1 - \frac{V(a)}{V(h)}} \int_0^\pi \left(1 - \frac{V(a) \sin^2 \phi - V(a/\sin \phi)}{2V(h) \cos^2 \phi} + O\left(\frac{V(a)^2}{V(h)^2}\right) \right) d\phi \quad (\text{C1})$$

Also expanding the $\sqrt{\dots}$ prefactor gives

$$\Theta \underset{a \gg h}{=} \frac{\pi}{2} \frac{V(a)}{V(h)} + \frac{1}{2} \int_0^\pi \frac{V(a) \sin^2 \phi - V(a/\sin \phi)}{V(h) \cos^2 \phi} d\phi + O\left(\frac{V(a)^2}{V(h)^2}\right) \quad (\text{C2})$$

For inverse power potentials the remaining integrand is

$$\frac{V_n(a) \sin^2 \phi - V_n(a/\sin \phi)}{V_n(h) \cos^2 \phi} = \frac{h^n \sin^2 \phi - \sin^n \phi}{a^n \cos^2 \phi} \quad (\text{C3})$$

which leads to an n -dependent integral without any further dependence on h or a .

$$\Theta \underset{a \gg h}{=} \frac{h^n}{a^n} \left(\frac{\pi}{2} + \frac{1}{2} \int_0^\pi \frac{\sin^2 \phi - \sin^n \phi}{\cos^2 \phi} d\phi \right) + O\left(\frac{h^{2n}}{a^{2n}}\right) \quad (\text{C4})$$

Note the integrand vanishes when $n = 2$. Otherwise, direct evaluation of this last integral gives⁵

$$\frac{1}{2} \int_0^\pi \frac{\sin^2 \theta - \sin^n \theta}{\cos^2 \theta} d\theta = \frac{\sqrt{\pi} \Gamma\left(\frac{n+1}{2}\right)}{\Gamma\left(\frac{n}{2}\right)} - \frac{\pi}{2} \quad (\text{C5})$$

and hence the power-law potential result given in the text:

$$\Theta \underset{a \gg h}{=} \frac{h^n}{a^n} \frac{\sqrt{\pi} \Gamma\left(\frac{n+1}{2}\right)}{\Gamma\left(\frac{n}{2}\right)} + O\left(\frac{h^{2n}}{a^{2n}}\right) \quad (\text{C6})$$

By comparison, the small scattering angle approximation for a Yukawa potential leads to an integral that is more challenging. Let $V(r) = \frac{\kappa}{r} \exp(-r/\lambda)$ to find

$$\Theta \underset{a \gg h}{=} \frac{h}{2a} \exp\left(\frac{h-a}{\lambda}\right) \left(\pi + \int_0^\pi \frac{\sin \phi}{\cos^2 \phi} \left(\sin \phi - \exp\left(\frac{a}{\lambda} \left(1 - \frac{1}{\sin \phi}\right)\right) \right) d\phi \right) + O\left(\frac{V(a)^2}{V(h)^2}\right) \quad (\text{C7})$$

and eventually obtain, in Maple notation,

$$\Theta \underset{a \gg h}{=} \frac{h}{a} \exp\left(\frac{h-a}{\lambda}\right) \left(-3 + \sqrt{8\pi a/\lambda} \operatorname{hypergeom}\left(\left[-\frac{1}{2}, \frac{3}{2}\right], \square, -\frac{\lambda}{2a}\right) \right) + O\left(\frac{V(a)^2}{V(h)^2}\right) \quad (\text{C8})$$

For fixed λ , small angle scattering is again obtained for $a \approx s \gg h$ or λ . But in this limit the hypergeometric function simplifies to $\lim_{\lambda/a \rightarrow 0} \operatorname{hypergeom}\left(\left[-\frac{1}{2}, \frac{3}{2}\right], \square, -\frac{\lambda}{2a}\right) = 1$. Thus

$$\Theta \underset{a \approx s \gg h, \lambda}{\sim} \sqrt{\frac{8\pi}{s\lambda}} h \exp\left(-\frac{s}{\lambda}\right), \quad \frac{d}{ds} \Theta \underset{a \approx s \gg h, \lambda}{\sim} -\frac{1}{\lambda} \sqrt{\frac{8\pi}{s\lambda}} h \exp\left(-\frac{s}{\lambda}\right) \quad (\text{C9})$$

$$\frac{s}{\lambda} \underset{\Theta \ll 1}{\sim} \frac{8\pi h^2}{\Theta^2 \lambda^2} \exp\left(-\operatorname{LambertW}\left(\frac{16\pi h^2}{\Theta^2 \lambda^2}\right)\right) \quad (\text{C10})$$

as used in the text. Also recall $\operatorname{LambertW}(w) \underset{w \gg 1}{\sim} \ln w - \ln \ln w + o(1)$, so $w \exp(-\operatorname{LambertW}(w)) \underset{w \gg 1}{\sim} O(\ln w)$.

⁵Therein lies a tale. For even $n = 2k$, a generating function for such integrals is given by

$$\frac{2}{\pi x} \sum_{k=1}^{\infty} x^k \left(\frac{\sqrt{\pi} \Gamma\left(\frac{2k+1}{2}\right)}{\Gamma(k)} - \frac{\pi}{2} \right) = \frac{1}{(1-x)^{3/2}} - \frac{1}{1-x}$$

See <https://oeis.org/A173384>.

References

- [1] For some previous work on this subject, albeit only for the Coulomb potential, please see the following six references.
- [2] John W. Adolph, A. Leon Garcia, William G. Harter, G. C. McLaughlin, Richard R. Shiffman, and Victor G. Surkus, “Some Geometrical Aspects of Classical Coulomb Scattering” *Am. J. Phys.* 40 (1972) 1852–1857.
- [3] R. E. Warner and L. A. Huttar, “The parabolic shadow of a Coulomb scatterer” *Am. J. Phys.* 59 (1991) 755–756.
- [4] Petar Zugec and Ivan Topic, “A shadow of the repulsive Rutherford scattering in the fixed-target and the center-of-mass frame” *Eur. J. Phys.* 41 (2020) 065005.
- [5] D. A. Shatilov and Z. K. Silagadze, “A shadow of the repulsive Rutherford scattering and Hamilton vector” *Eur. J. Phys.* 42 (2021) 035001.
- [6] Jie Gu and Chang-Cai Chen, “A geometric approach to the envelope of Coulomb orbits starting from a point in space” *Eur. J. Phys.* 42 (2021) 055007.
- [7] Petar Zugec and Dario Rudec, “A shadow of the repulsive Rutherford scattering in the laboratory frame” *Eur. J. Phys.* 42 (2021) 055018.
- [8] James E. Harvey and James L. Forgham, “The spot of Arago: New relevance for an old phenomenon” *Am. J. Phys.* 52 (1984) 243–247; Olivier Emile and Janine Emile, “The Arago–Poisson Spot: New Applications for an Old Concept” *Photonics* 11 (2024) 55.
- [9] Thomas Reisinger, Amil A. Patel, Herbert Reingruber, Katrin Fladischer, Wolfgang E. Ernst, Gianangelo Bracco, Henry I. Smith, and Bodil Holst, “Poisson’s spot with molecules” *Phys. Rev. A* 79 (2009) 053823.